Characterization of Nanomaterials by Physical Methods

C.N.R. Rao[1,2] and Kanishka Biswas[1,2]

[1]Chemistry and Physics of Materials Unit, DST Nanoscience Unit, and CSIR Center of Excellence in Chemistry, Jawaharlal Nehru Center for Advanced Scientific Research, Bangalore 560064, India; email: cnrrao@jncasr.ac.in

[2]Solid State and Structural Chemistry Unit, Indian Institute of Science, Bangalore 560012, India

Annu. Rev. Anal. Chem. 2009. 2:435–62

First published online as a Review in Advance on April 6, 2009

The *Annual Review of Analytical Chemistry* is online at anchem.annualreviews.org

This article's doi:
10.1146/annurev-anchem-060908-155236

1936-1327/09/0719-0435$20.00

Key Words

electron microscopy, scanning probe microscopies, diffraction, nanocrystals, nanowires, nanotubes

Abstract

Much progress in nanoscience and nanotechnology has been made in the past few years thanks to the increased availability of sophisticated physical methods to characterize nanomaterials. These techniques include electron microscopy and scanning probe microscopies, in addition to standard techniques such as X-ray and neutron diffraction, X-ray scattering, and various spectroscopies. Characterization of nanomaterials includes the determination not only of size and shape, but also of the atomic and electronic structures and other important properties. In this article we describe some of the important methods employed for characterization of nanostructures, describing a few case studies for illustrative purposes. These case studies include characterizations of Au, ReO_3, and GaN nanocrystals; ZnO, Ni, and Co nanowires; inorganic and carbon nanotubes; and two-dimensional graphene.

1. INTRODUCTION

Characterization of nanomaterials is performed at different levels. Some characterization methods are used to study the sizes, shapes, and morphology of nanostructures, whereas others are used to obtain detailed structural information. The structures of materials can be studied at various levels of sophistication, including crystal structure, microstructure, atom-level structure, and electronic structure. X-ray and neutron diffraction are routinely used for determination of crystal structure, and the use of synchrotron X-ray radiation and pulsed neutrons, along with Rietveld analysis, has made these techniques more powerful. X-ray diffraction (XRD) is also used to obtain the average size of the particles via the Scherrer formula:

$$a = 0.9\lambda / B \cos\theta,$$

where a is the particle size, λ is the X-ray wavelength, B is the full width of the half maxima (in radians) of the X-ray peak, and θ is the Bragg angle. Neutron diffraction is particularly useful for the study of nanostructures of ceramic materials such as metal oxides. The study of hydrogen in hydrides or on specific sites or pores of materials is best carried out by neutron diffraction or scattering. X-ray scattering is an invaluable technique for studying the distribution of shapes and sizes of the nanocrystals. Several techniques, including X-ray photoelectron spectroscopy (XPS), provide information about the electronic structure of nanomaterials. Transmission electron microscopy (TEM) is employed not only to determine a nanomaterial's size, shape, and crystal structure, but also to unravel the composition and electronic structure via in situ techniques such as electron energy-loss spectroscopy (EELS). Additionally, scanning probe microscopies have become invaluable in the study of nanostructures. These techniques help not only to characterize nanostructures, but also to manipulate them and allow examination of their properties. Furthermore, techniques such as Raman spectroscopy are invaluable when used with other techniques. Spectroscopic properties of nanostructures are employed to investigate their characteristics and some of the phenomena they exhibit. For example, electronic emission spectroscopy [e.g., photoluminescence (PL)] is extensively employed to characterize quantum dots that can be used in a variety of applications.

In this review, we briefly describe some of the important techniques employed for the characterization of nanostructures, giving typical examples in each case. There are techniques that we do not cover; therefore, we describe a few typical case studies involving a variety of physical methods to demonstrate how characterization of nanomaterials requires diverse techniques.

Rietveld profile analysis: method used to determine the structure of powder materials by employing profile analysis of the experimental diffraction data. The results so obtained are often as good as those obtained by single-crystal diffraction techniques

XRD: X-ray diffraction

XPS: X-ray photoelectron spectroscopy

TEM: transmission electron microscopy

PL: photoluminescence

2. CHARACTERIZATION TECHNIQUES

2.1. Powder X-Ray Diffraction

XRD is the most essential tool used to characterize crystal structures. Evaluation of crystal structure is important even for nanoscale materials (1, 2). Although a material's properties may be affected by structures on the nanometer scale, its crystal structures are determined by the arrangement of atoms separated from one another by approximately 0.1 nm. The principle of powder XRD is based on the well-known Bragg's law ($\lambda = 2d \sin\theta$). The most commonly used database for the identification of crystal structures is the Joint Committee on Powder Diffraction Standards–International Center for Diffraction Data (JCPDS-ICDD) system. Rietveld profile analysis (3) of experimental XRD patterns provides information about a given material's space group and structural parameters. **Figure 1** shows the pressure-dependent XRD patterns of 4.4-nm-diameter CdSe nanocrystals under compression and decompression (4). CdSe nanocrystals show a wurtzite-to-zincblende phase transition at an upstroke pressure of 6.3 GPa, which is twice the

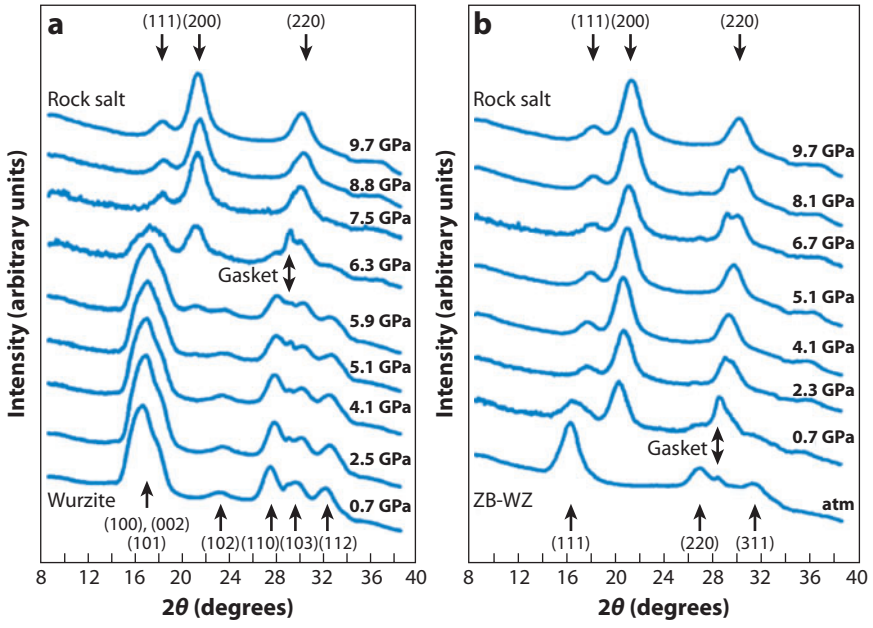

Figure 1

Changes in X-ray diffraction (XRD) patterns for 4.4-nm-diameter CdSe nanocrystals for (*a*) compression and (*b*) decompression. ZB-WZ refers to a mixture of closely related zincblende and wurtzite structure. Labeled arrows indicate XRD from a high-pressure cell-metal gasket. The X-ray wavelength is 0.9939 Å. Reprinted from Reference 4 with permission. Copyright 2005, AAAS.

upstroke pressure of approximately 3 GPa for bulk CdSe. In general, the XRD peaks of nanocrystals are much broader compared to those of the bulk.

Evaluation of the average crystallite size using the Scherrer formula (1, 2) is an important application of powder XRD in the study of nanomaterials. For example, in the case of MnO (5), CoO (6), NiO (5), and ReO_3 (7) nanocrystals, Rietveld profile analysis and the Scherrer formula were employed to determine the structure and average particle size. In the case of doped nanomaterials, it is often possible to obtain the extent of doping from the shifts in the XRD reflections. Although XRD is routinely carried out with standard laboratory diffractometers, it may be necessary to use synchrotron X-rays to obtain better resolution and sensitivity for materials such as metal oxides.

2.2. Electron Microscopies

Electron microscopes use electrons instead of photons because the former have shorter wavelengths, allowing the observation of matter with atomic resolution. There are two general types of electron microscopes. In a TEM, electrons are shot through the sample, and changes in the electron beam arising from scattering by the sample are measured. In a scanning electron microscope (SEM), the electron beam is scanned over the surface of an object to measure the electrons that are scattered back.

In a TEM, the incident electron beam is allowed to transmit through a thin sample at a high-acceleration voltage, whereupon the interaction between the sample and the electron beam gives rise to images (1, 2, 8). The spatial resolution in a modern TEM is less than 10^{-1} nm, with an

SEM: scanning electron microscopy

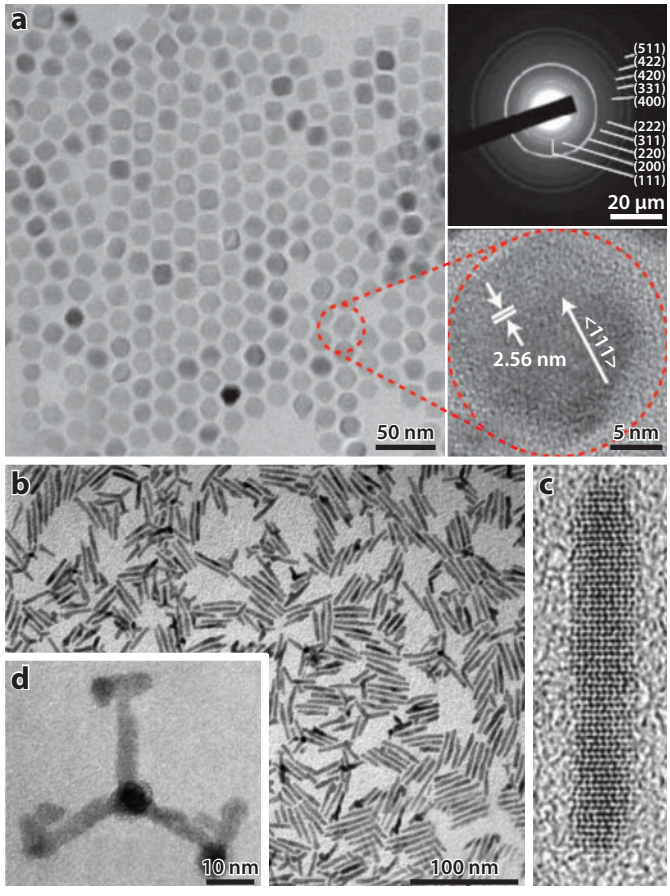

Figure 2

(*a*) Transmission electron microscopy (TEM) images, high-resolution TEM (HREM) images, and electron diffraction patterns of monodisperse MnO nanocrystals. The lower right panel shows a lattice corresponding to the (111) planes of cubic MnO, and the upper right panel shows a selected area electron diffraction pattern of MnO nanocrystals. (*b*) TEM images of CdSe nanorods with an aspect ratio of 10:1. The sample contains less than 5% tetrapods. (*c*) HREM image of a single CdSe nanorod. (*d*) HREM image of a tetrapod with branches growing out of each arm. There are zincblende layers near the ends of the original arms, and the branches are made of wurtzite, with some stacking faults. Reprinted from References 9 and 10 with permission. Copyright 2004, Nature Publishing Group; copyright 2000, American Chemical Society.

Selected area electron diffraction (SAED): refers to elastically scattered electrons from a selected region of a nanomaterial. The electrons follow Bragg's law and form circular patterns (rings) rather than spots; each ring corresponds to a specific lattice spacing of the nanomaterials

electron probe size measuring less than 5×10^{-1} nm. From the difference between the contrast of the sample and the background, one can obtain direct information about the morphology of nanomaterials (**Figure 2**). If a microscope has a sufficiently high point resolution, and if the specimen is suitably oriented along the zone axis, high-resolution TEM (HREM) images can be obtained. In many cases, atomic structures and growth directions of nanomaterials can be directly investigated by HREM (**Figure 2**) (9, 10). **Figure 3** shows typical HREM images of the different types of carbon nanotubes (11–13).

Electron diffraction (ED) patterns obtained by TEM yield information about the orientations, atomic arrangements, and structures of narrow regions of interest in nanomaterials. A selected area electron diffraction (SAED) pattern of MnO nanocrystals (9) is depicted in **Figure 2*a***. Diffuse rings in the SAED pattern correspond to different lattice planes of cubic MnO.

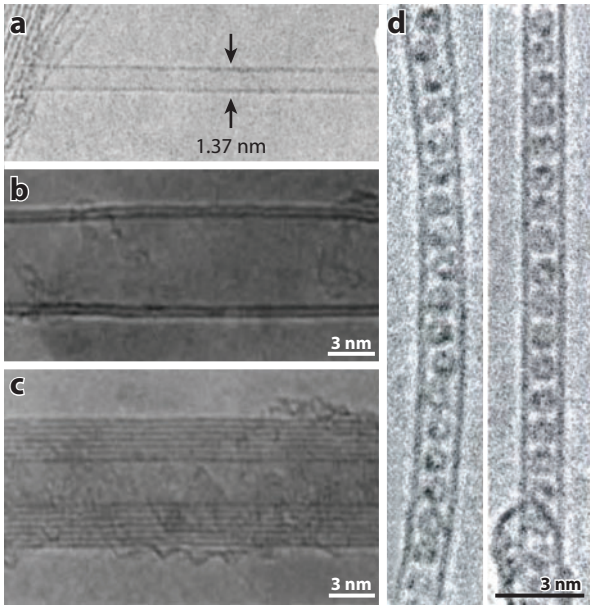

Figure 3

Typical high-resolution transmission electron microscopy (HREM) images of (*a*) a single-walled nanotube (SWNT), (*b*) a double-walled nanotube (DWNT), and (*c*) a multiwalled nanotube (MWNT). (*d*) HREM images of the isolated SWNT containing the $Gd@C_{82}$ fullerenes (the so-called peapods). Reprinted from References 11, 12, and 13 with permission. Copyright 1993 and 1991, Nature Publishing Group; copyright 2000, American Physical Society.

EELS, which makes use of the inelastic scattering of the incident electrons on the sample, is an important tool for qualitative and quantitative analysis of elements (14). It also unravels aspects related to chemical bonding in very small regions of the sample. The EELS technique is available via TEM; for example, composition and elemental analysis of B-C-N, C-N, B-N, and nanotubes have been carried out by EELS (15, 16).

SEM produces images by focusing a high-energy electron beam onto the surface of the sample, then detecting signals from the interaction of the incident electrons with the sample's surface (17). SEM images have great depth of field, yielding a characteristic three-dimensional appearance that is useful for understanding the surface structure of a sample. The spatial resolution of a SEM image depends on the size of the electron spot, which in turn depends on both the wavelength of the electrons and the magnetic electro-optical system that produces the scanning beam. Both the spot size and the interaction volume may be large compared to the distances between atoms; the resolution of the SEM, therefore, is not high enough to image individual atoms (as can be done with TEM). However, SEM has other advantages, including the ability to image a relatively larger area of samples and to image bulk materials such as thin films and foils. Depending on the instrument, the resolution of SEM may be anywhere between <1 nm and 20 nm.

2.3. Scanning Probe Microscopies

2.3.1. Atomic force microscopy. Atomic force microscopy (AFM) is one of the scanning probe microscopies employed for imaging surface profiles (18). A typical horizontal distance resolution is approximately 0.2 nm. AFM can provide a resolution higher than that of typical SEM and comparable to that of TEM.

AFM: atomic force microscopy

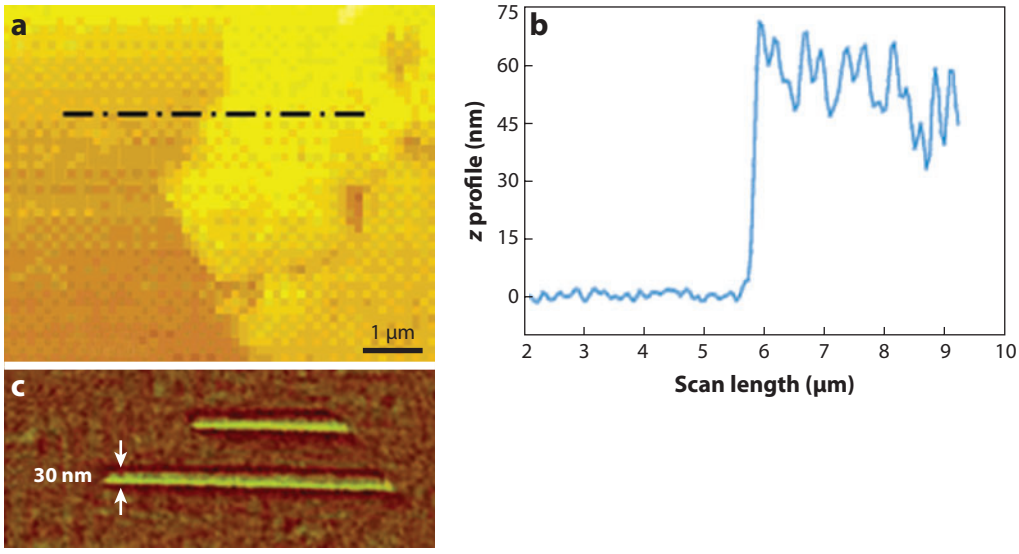

Figure 4

(*a*) Contact mode atomic force microscopy (AFM) image showing the boundary of Au film on a mica substrate. (*b*) The *z* profile of the film boundary. The height profile estimates the thickness to be ~60 nm, which corresponds to approximately eight monolayers of nanocrystals. The jagged line profile (*right*) corresponds to the variation in the film thickness, with trenches of ~7 nm indicating missing particles in the top layer. (*c*) Contact mode AFM image of an Au nanocrystal pattern drawn on mica substrate by dip-pen lithography. Reprinted from References 19 and 20 with permission. Copyright 2005, American Chemical Society; copyright 2004, Royal Society of Chemistry.

AFM provides real topographical images of sample surfaces. A typical vertical distance resolution is 0.01 nm, which is superior to those of SEM and TEM (2, 18). In a typical AFM setup, the deflection of a microfabricated cantilever with a sharp tip is measured by reflecting a laser beam from the back side of the cantilever as it scans over the surface of the sample. Several variants of AFM are used to measure topography and investigate surface forces on the nanoscale. In contact mode AFM, the tip in contact with the substrate provides high-resolution images but can damage fragile surfaces. In tapping or intermittent contact mode AFM, the tip oscillates and taps the surface. In non–contact mode AFM, the tip oscillates but does not touch the sample. **Figure 4*a*** shows contact mode AFM images of a nanocrystalline gold film, prepared at the toluene-water interface, on mica substrate (19). Such imaging is possible to carry out in air, liquid, vacuum, and gas. AFM techniques are used to measure surface properties such as the frictional force on the nanoscale, the hardness of surfaces, surface charge distribution, surface magnetization, yield stress, and the elastic plastic deformation dynamics of nanomaterials. AFM is also used as a lithographic technique as in dip-pen lithography (**Figure 4*c***) (20). Using the conducting cantilever probe in contact mode AFM (a technique known as conducting AFM), one can obtain current (*I*) versus voltage (*V*) measurements of a given nanomaterial. H_2 and liquid petroleum gas sensors have been fabricated based on WO_3, ZnO, and TiO_2 nanowires to carry out *I–V* measurements by conducting AFM (21).

STM: scanning tunneling microscopy

2.3.2. Scanning tunneling microscopy. Scanning tunneling microscopy (STM) is a powerful technique for viewing surfaces at the atomic level (18). Using a tunneling current, STM probes the density of the states of a material. When a conducting tip is brought near a metallic or

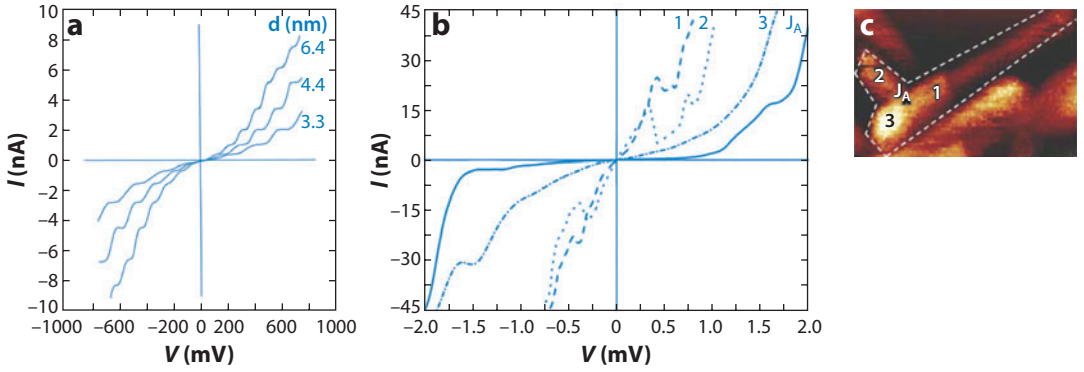

Figure 5

(*a*) Current versus voltage (*I–V*) data of isolated Pd nanocrystals of different sizes. The step width, which is 208 mV for the 3.3-nm nanocrystal, decreases to 158 mV for the 4.4-nm nanocrystal and to 116 mV for the 6.4-nm nanocrystal. (*b*) *I–V* data of N-doped Y-junction carbon nanotubes. The data obtained at the Y-junction exhibit rectification behavior, with a distinct change of slope at −1.5 V and +1 V. A high rectification ratio of 4.75 is obtained for a bias voltage of ± 1.5 V. (*c*) Scanning tunneling microscopy images. The *I–V* data-collection regions are marked with numbers. Reprinted from References 22 and 23 with permission. Copyright 2000 and 2005, Elsevier.

semiconducting surface, a bias allows electrons to tunnel through the vacuum between them. For low voltages, this tunneling current is a function of the local density of states at the Fermi level of the sample. Variations in the current as the probe passes over the surface are transformed into an image. In STM, ~0.1 nm is a good lateral resolution and 0.01 nm is a good depth resolution. STM is useful for obtaining information about the electronic states and the morphology of nanomaterials of different dimensionalities. The *I–V* data of isolated polyvinylpyrrolidone (PVP)-capped Pd nanocrystals of different sizes (**Figure 5*a***) indicate the occurrence of Coulomb staircase phenomena at room temperature in tunnel junctions (22). **Figure 5*b*** depicts the *I–V* data of a junction of N-doped Y-junction carbon nanotubes (23).

2.4. Small-Angle X-Ray Scattering

Small-angle X-ray scattering (SAXS) enables evaluation of the sizes of small particles or the modulation of the electron density ranging from several to 100 nm by analyzing the scattered intensity of X-rays in a small angular range from approximately 0.1° to 3° (24, 25). In contrast to XRD, SAXS can be applied not only to crystalline materials but also to amorphous materials, polymers, and biomolecules. The SAXS intensity depends on the electron density and the form factor [$F(q)$]: $q = 4\pi \sin\theta/\lambda$, where θ is the scattering angle and λ is the wavelength of the X-ray of the particle and the structure factor [$S(q)$] (24, 25). The most basic application of SAXS is the evaluation of the particle size, shape, orientation, and size distribution in dilute dispersions, where the particle-particle correlation factor, $S(q)$, is negligible. In order to evaluate particle size distribution, experimental SAXS data are fitted to a theoretical model (**Figure 6*a***) (26).

SAXS is also used to obtain information about the inhomogeneity within amorphous materials and the pore sizes in porous materials. Analysis of SAXS data has been employed to evaluate long-range ordering or interparticle distances in an assembly of nanocrystals or in polymeric materials. To obtain good resolution in the SAXS data, one must use a high-energy X-ray source such as a synchrotron.

SAXS: small-angle X-ray scattering

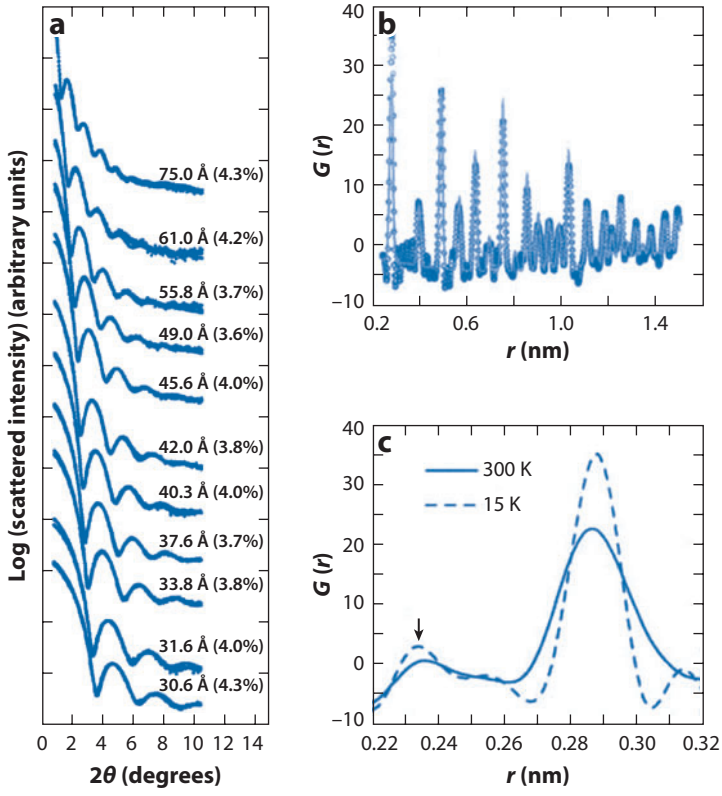

Figure 6

(*a*) Small-angle X-ray scattering (SAXS) patterns for CdSe nanocrystals ranging from 30 to 75 Å in diameter (*dots*). Also shown are computer simulation data (*solid lines*) used to obtain the size distribution of CdSe nanocrystals. Fits are used to devise the NC sample size, reported in equivalent diameters, and size distributions, ranging from 3.5 to 4.5% for the samples shown. (*b*) Pair-distribution functions (PDF) of gold nanocrystals at 15 K. The filled circles represent the experimental data, and the solid line indicates the model PDF. (*c*) The nearest-neighbor region of the PDF. The sharp intense peak at 2.8 Å is due to the shortest Au-Au distance, and the peak at 2.4 Å is due to the Au-S (gold to capping thiol) distance. A structural feature at $r = 0.235$ nm is marked by an arrow. Reprinted from References 26 and 28 with permission. Copyright 2000, Annual Reviews; copyright 2004, Elsevier.

2.5. Pair-Distribution Functions

In many materials, especially those with intermediate-range order, structural coherence disappears at the nanometer scale, making it difficult to obtain structural solutions by standard crystallographic techniques. Significant advances have recently been made in the use of atomic pair-distribution function (PDF) analysis of powder diffraction data coupled with the use of advanced high-energy X-ray and neutron sources and fast computers (27). The PDF technique makes use of the Fourier relationship between the diffraction intensities and the real-space arrangement of pairs of atoms. The PDF can be defined in real space in terms of atomic coordinates. Because the peaks in the PDF arise from pairs of atoms in the material, a peak shifted to a lower-r (i.e., lower distance) indicates that the pairs of atoms have a shorter bond. PDF analysis of X-ray and neutron diffraction data, which account for both the Bragg and the diffuse components of scattering, are used to solve structures of nanomaterials, amorphous materials, and gels, which cannot otherwise

PDF: pair-distribution function

be examined by traditional crystallographic techniques. PDF analysis gives local structural information on a material that cannot be obtained by crystallography. In **Figure 6*b–c***, we show the neutron PDF data of fluorothiol-capped gold nanoparticles measuring 4 nm in diameter (28). It is possible to obtain other structural information, such as lattice parameters, from model fits to the experimental data.

2.6. Energy-Dispersive X-Ray Analysis

Energy-dispersive X-ray spectroscopy (EDAX) is used mainly for elemental analysis and for chemical characterization of samples (17). The technique is based on the fact that every element has a unique atomic structure such that X-rays characteristic of different atomic structures are readily distinguishable from one another. In EDAX, the incident electron beam excites an electron in an inner shell, causing its ejection and the formation of an electron hole in the electronic structure of the atom. An electron from a higher-energy (outer) shell fills the hole, and the difference in energy between the higher-energy shell and the lower-energy shell is released as X-rays. The X-rays thus released are analyzed by means of an energy-dispersive spectrometer. EDAX systems are commonly found with SEM, as well as with TEM. For example, EDAX has been used to obtain elemental analysis of Au-Ag-alloy nanocrystalline films generated at the liquid-liquid interface (29).

2.7. X-Ray Photoelectron Spectroscopy

XPS is a quantitative technique that measures the elemental composition, empirical formula, chemical state, and electronic state of the elements within a nanomaterial (1, 2). Spectra are obtained by irradiating a given material with a beam of Al or Mg X-rays and simultaneously measuring the kinetic energy and number of electrons that escape from the top 1–10 nm of the material. XPS requires ultrahigh vacuum. For example, XPS analysis indicates the presence of B and N in B-C-N nanotubes and reports the composition as $BC_{28}N$ (15). Photoelectron spectroscopy techniques, which include XPS, can be divided into two subgroups according to the exciting radiation. Specifically, (*a*) XPS uses soft X-rays (200–2000 eV) to examine core levels (inner-shell electrons), whereas (*b*) ultraviolet (UV) photoelectron spectroscopy employs UV radiation to investigate valence levels (outer-shell electrons). Thus, valence bands and changes in the Fermi level of materials can be effectively studied by UV photoelectron spectroscopy.

2.8. Electronic Absorption Spectroscopy

Electronic absorption spectroscopy involves measuring the attenuation of a beam of light after it passes through a sample or after it is reflected from the sample surface (1, 2). This attenuation may arise from absorption, scattering, reflection, or interference. The simplest optical measurements are transmission (absorption) and reflectivity. For transmission measurements in wavelengths ranging from 150 nm (ultraviolet) to 3000 nm (near-infrared), commercially available dual-beam spectrophotometers may be used. One can obtain information about the size and shape of metal nanocrystals by measuring the position and nature of the surface plasmon absorption bands in the UV-visible region. In the case of semiconducting nanocrystals, electronic spectra are directly related to the band gap of the materials. Thus, with decreasing diameter, a blueshift of the band edge absorption appears. **Figure 7*a*** shows the UV-visible spectra of monodisperse CdSe nanocrystals (26), and **Figure 7*b*** shows the diameter versus band edge peak position plots for CdS, CdSe, and CdTe nanocrystals (30).

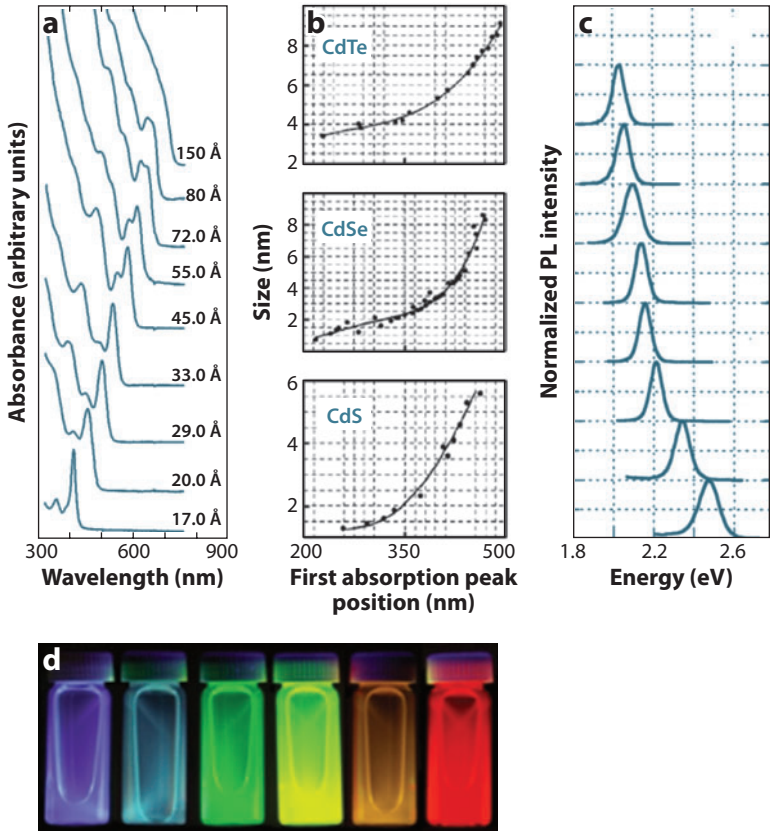

Figure 7

(*a*) Optical absorption spectra for a series of monodisperse CdSe nanocrystals ranging in diameter from 1.7 to 15 nm. The blueshift of the absorption edge occurs progressively with decreasing particle size. (*b*) First absorption peak change versus the size of CdS, CdSe, and CdTe nanocrystals. The curves depicted enable one to estimate the average diameter of semiconductor nanocrystals from the optical band edge peak position, or vice versa. (*c*) Photoluminescence (PL) spectra of CdSe nanocrystals with diameters ranging from 2.4 to 4.4 nm. The band edge luminescence of these nanocrystals shifts to lower energy with decreasing diameter. Reprinted from References 26, 30, and 32 with permission. Copyright 2000, Annual Reviews; copyright 2003, American Chemical Society; copyright 1998, American Chemical Society. (*d*) Fluorescence induced by exposure to ultraviolet light in vials containing CdSe quantum dots of various sizes. Data taken from **http://nanocluster.mit.edu/research.php**.

UV-visible spectroscopy is also useful for tracking the in situ growth kinetics of small semiconductor nanocrystals such as CdSe and CdS (31). It is also an important tool for obtaining information about the electronic structure of carbon nanotubes.

2.9. Photoluminescence

PL spectroscopy is a powerful technique for investigating the electronic structure of both intrinsic and extrinsic semiconducting nanomaterials (1, 2). The PL spectrum provides information about a sample's quality and is helpful in determining impurity concentration, identifying defect complexes, and measuring the band gaps of semiconductors. When a semiconductor is excited by a

light source with a photon energy greater than the band gap energy of the material, electrons are promoted to the conduction band and leave holes behind. When the electron-hole pair recombines, it emits a photon that has a wavelength characteristic of the material and the particular radiative process involved. **Figure 7*c*** shows the PL spectra of CdSe nanocrystals at different times after growth (32). A PL spectrum (as of the nanocrystals in **Figure 7*c***) can be translated into a size distribution curve by assuming a δ function emission for each single size and the same emission efficiency for different sizes (32). Imaging luminescence from individual nanocrystals has also been achieved via dilution of nanocrystal solutions. Useful information can be obtained from the time dependence and the efficiency of luminescence. A pulsed-laser source and a gated detection in time-resolved PL can provide details about the energies and lifetimes of the trap states.

2.10. Raman Spectroscopy

Raman spectroscopy is based on the inelastic scattering of light by matter. It probes the structures of gases and liquids as well as those of amorphous and crystalline solids. Raman activity is a function of the space group symmetry of a crystalline solid. It provides a wide range of information about the strength of interatomic and intermolecular bonds within the material, mechanical strain, the material's degree of crystallinity, and the effects of pressure and temperature (33). The incident radiation induces transitions in the atoms or molecules in the scattering medium. The transitions can be rotational, vibrational, electronic, or a combination of these. In general, a Raman spectrum plots the intensity of the inelastically scattered light as a function of the shift of the radiation in wave number. Each peak in the spectrum corresponds to one or more vibrational modes of the nanostructures. Because carbon exists in a variety of solid forms ranging from diamond to graphite to amorphous carbon, Raman spectroscopy is most effective in characterizing carbon nanostructures and is extensively used to study carbon nanotubes (34). If a scattering system has an absorption band close to the excitation frequency, resonance Raman scattering (RRS) results (33). The intensity of RRS is generally several orders of magnitude greater than that of normal Raman scattering. RRS is common in the case of carbon nanotubes. Surface-enhanced Raman scattering (SERS) is employed to detect adsorbed molecules on metal nanocrystal surfaces at the parts-per-million level (33, 35).

2.11. Magnetic Characterization

Magnetic characterization of nanomaterials is generally carried out with a vibrating sample magnetometer (VSM) or with a superconducting quantum interference device (SQUID) (1). The most common VSMs use a transverse-coil configuration, where the vibration (z) axis is perpendicular to the field applied by the electromagnet and where the pickup coils are arranged to sense the moment along the field direction. For higher fields, transverse-field superconducting magnets are used. A SQUID is an extremely low-impedance, high-sensitivity flux detector that can operate over a wide range of frequencies. The magnetometer detects the flux produced by a sample passing through a pickup coil. The SQUID does not measure the field from the sample directly, but it is coupled inductively to a superconducting pickup coil located in the high-field region. From these techniques, one can obtain magnetization versus temperature or magnetization versus field data.

Superparamagnetism: phenomenon by which magnetic materials may exhibit a behavior similar to paramagnetism even when at temperatures below the Curie or Néel temperature

Ferromagnetic materials generally show a decrease in transition temperature with a decrease in particle size. When the particle size is very small (<10–15 nm), the particles become superparamagnetic. Nanocrystals of many materials show evidence of the presence of ferromagnetic interactions at low temperatures. This is especially true of nanocrystals of antiferromagnetic oxides

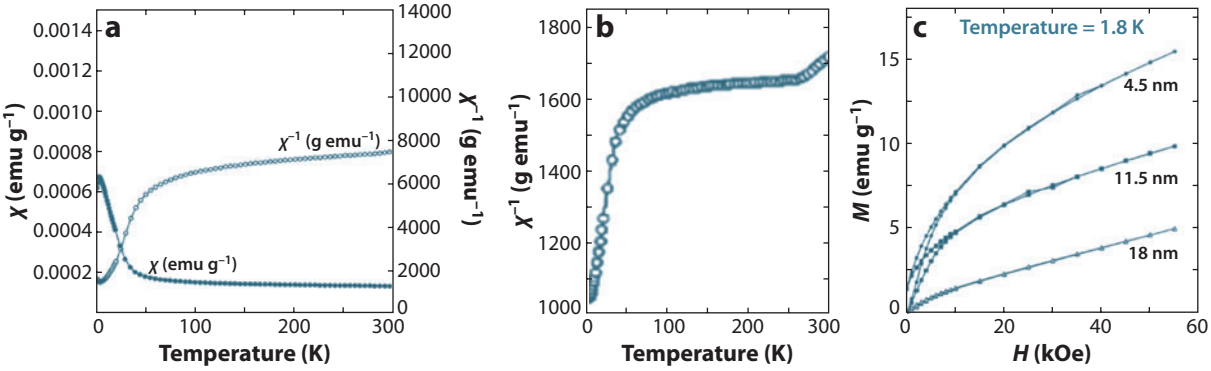

Figure 8

(*a*) The temperature dependence of direct current magnetic susceptibility (χ) and the inverse magnetic susceptibility (χ^{-1}) of 11.5-nm CoO nanocrystals. (*b*) The inverse susceptibility versus temperature curve of 16-nm CoO. The Curie-Weiss temperature (Θ_p) values are –1894, –1030, and –300 K for the 11.5-, 8.5-, and 4.5-nm samples, respectively; the magnetic moments are close to 5 μB. (*c*) Magnetization (*M*) versus field (*H*) at 1.8 K for 4.5-, 11.5-, and 18-nm CoO nanocrystals. Hysteresis does not occur in the 18-nm sample. Reprinted from Reference 6 with permission. Copyright 2005, American Chemical Society.

such as MnO, CoO, and NiO (5, 6). Thus, 16-nm or 18-nm particles of CoO reveal the presence of an antiferromagnetic transition, as evidenced by a broad peak at approximately 300 K in the inverse susceptibility data (**Figure 8*b***). The antiferromagnetic transition is wiped out as the particle size decreases due to the increased ferromagnetic interaction with decrease in particle size (**Figure 8*a***). Accordingly, the magnitude of the Curie-Weiss temperature obtained from the extrapolation of the high-temperature inverse susceptibility data decreases with the increase in particle size. Samples of 4.5- and 11.5-nm diameters show hysteresis at low temperatures below a blocking temperature, T_B, due to superparamagnetism (**Figure 8*c***). The blocking temperature increases with the rise in particle size in the case of NiO and exhibits the reverse trend in the case of MnO (5). Room-temperature ferromagnetism has been observed even in nanocrystals of nonmagnetic materials, including CeO_2, Al_2O_3, ZnO, In_2O_3, SnO_2, GaN, and CdS (36, 37). All of these materials showed characteristic magnetic hysteresis that was not found in the bulk samples. Given that no magnetic impurities were present, the origin of ferromagnetism may be the exchange interactions between the localized electron spin moments that result from anion or cation vacancies at the surfaces of nanocrystals. Thus, ferromagnetism may indeed be a universal characteristic of nanocrystals.

Electron paramagnetic resonance is employed to characterize paramagnetic centers due to transition metal ions, defects, etc. Nuclear magnetic resonance spectroscopy can be effectively employed to study phenomena in nanomaterials, provided there are appropriate nuclei with precise spins. For examples, water in carbon nanotubes is studied by variable-temperature nuclear magnetic resonance (38).

2.12. Other Techniques

Several other techniques are employed to characterize nanomaterials. For instance, mass spectroscopy is used to determine the nuclearity of metal clusters. Infrared spectroscopy covers a range of techniques, most commonly a form of absorption spectroscopy that is frequently used to identify molecules covering nanomaterial surfaces (1). Infrared spectroscopy of materials provides

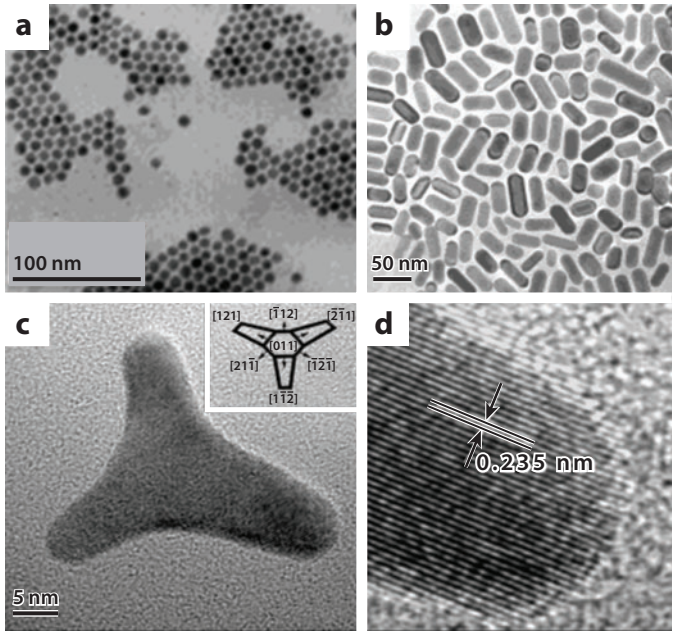

Figure 9

Transmission electron microscopy (TEM) images of (*a*) spherical, (*b*) rod-shaped, and (*c*) tripod-shaped gold nanocrystals. (*d*) High-resolution TEM (HREM) image of an arm of a tripod-shaped Au nanocrystal, which exhibits (111) planes with an interplanar distance of 0.235 nm. Analysis of the growth directions for the three pods, which are separated from one another by approximately 120°, shows that the orientation of the crystallite is [011] and that the possible growth directions are of <211> type. (*Inset in c*) The crystal planes and the tripod growth directions extracted from the HREM analysis. The pods extend in [1$\bar{1}$2], [2$\bar{1}$1], and [121] directions. Reprinted from References 41, 42, and 43 with permission. Copyright 2003, 2002, and 2005, American Chemical Society.

information complementary to that provided by Raman spectroscopy. Isothermal titration calorimetry (ITC) measures small changes in enthalpy arising from reactions involving nanostructures, such as the assembly of nanocrystals (39) and the binding of nucleobases with the nanotube (40). Electrical properties such as resistivity, thermopower, and the Hall effect are measured wherever electron transport and related aspects are of relevance.

3. CASE STUDIES

3.1. Zero-Dimensional Nanocrystals

3.1.1. Gold. TEM is one of the most important techniques used to characterize the sizes and shapes of gold nanocrystals. **Figure 9** shows TEM images of spherical (41), rod-shaped (42), and tripod-shaped (43) gold nanocrystals.

Colloidal solutions of gold nanocrystals exhibit characteristic colors due to the well-known phenomenon of surface plasmon absorption. As their size increases, spherical Au nanocrystals show redshift of the plasmon band to longer wavelengths (44). The plasmon resonance band of nanorods splits into transverse and longitudinal components (45). As the aspect ratio increases, the energy separation between two plasmon bands increases, with the longitudinal plasmon band

ITC: isothermal titration calorimetry

Surface plasmon resonance: caused by the coherent motion of the conduction band electrons of metals on interaction with the electromagnetic field

position shifting to a longer wavelength (46). The transverse band is insensitive to the aspect ratio.

SAXS is effective for tracking the in situ growth of gold particles in solution (47). The growth kinetics of gold nanocrystals cannot be explained by diffusion-limited Ostwald ripening (47, 48). In order to understand the thermodynamics of the growth of gold nanocrystals, the change in heat associated with the growth prepared with different concentrations of $HAuCl_4$ was measured by ITC (47). The interaction between gold nanorods with cysteine as well as with 3-mercaptopropionic acid to form necklaces has also been investigated by ITC (39).

I–V data of isolated PVP-capped gold nanocrystals of different sizes have been measured by STM (22). The curves are characteristic of metal-insulator-metal junctions, which are modulated on either side of the zero bias by a series of *I–V* steps. The *I–V* curves show characteristics of the Coulomb staircase.

Ultrathin nanocrystalline films of gold formed at different temperatures at the organic-aqueous interface have been investigated by XRD, TEM, AFM, and electronic spectroscopy (19). **Figure 10** shows TEM images, XRD patterns, and UV-visible spectra of the nanocrystalline gold films obtained at the liquid-liquid interface held at different temperatures.

3.1.2. ReO_3. ReO_3 is an unusual metal oxide: It has a cubic structure and exhibits metallic conductivity (49). It is comparable to copper in both appearance and electronic properties. Metallic ReO_3 nanocrystals exhibit a surface plasmon band of approximately 520 nm, which undergoes blueshifts as it decreases in size (**Figure 11*a***) (7). STM measurements of ReO_3 nanocrystals confirm their metallicity. Pressure-induced phase transitions in the nanocrystals of ReO_3 have been investigated in detail by using energy-dispersive high-pressure synchrotron XRD, and the results have been compared with the literature data of bulk samples of ReO_3 (50). Core@shell nanocrystals based on ReO_3 cores (ReO_3@SiO_2, ReO_3@TiO_2, ReO_3@Au, and ReO_3@Ag) have been characterized by TEM and electronic spectroscopy (51) (**Figure 11*b***). ReO_3@Au and ReO_3@Ag core-shell nanocrystals show composite plasmon absorption bands that comprise contributions from both ReO_3 and Au (Ag) (**Figure 11*b***), whereas ReO_3@SiO_2 and ReO_3@TiO_2 show shifts in their plasmon bands depending on the refractive index of the shell material.

SERS of pyridine, pyrazine, and pyrimidine on ReO_3 nanocrystals of three different sizes has also been performed recently (52). As with Au and Ag, the plasmon in ReO_3 can be utilized for SERS. The surface enhancement factor for pyridine adsorbed on ReO_3 nanocrystals is on the order of 10^6, which is comparable to the results for Au, Ag, and Cu (35).

3.1.3. GaN. Solvothermally prepared GaN nanocrystals of various sizes have been characterized by XRD, TEM, and PL spectroscopy (53). **Figure 12** shows typical TEM images of 2.5-nm *N*-cetyl-*N*,*N*,*N*-trimethylammonium bromide (CTAB)-capped GaN nanocrystals, a HREM image of a single CTAB-capped nanocrystal, and PL spectra of GaN nanocrystals of different sizes. Nanocrystals of GaN doped with 3% and 5% prepared at relatively low temperatures are found to be ferromagnetic above room temperature (54).

3.2. One-Dimensional Nanowires and Nanotubes

3.2.1. ZnO. ZnO nanostructures have potential applications as short-wavelength nanolasers, field-effect transistors, solar cells, ultrasensitive nanosized gas sensors, biosensors, nanoresonators, transducers, actuators, nanocantilevers, and field emitters (55). ZnO exhibits diverse nanostructures that are richer than most other nanomaterials. TEM characterization of ZnO

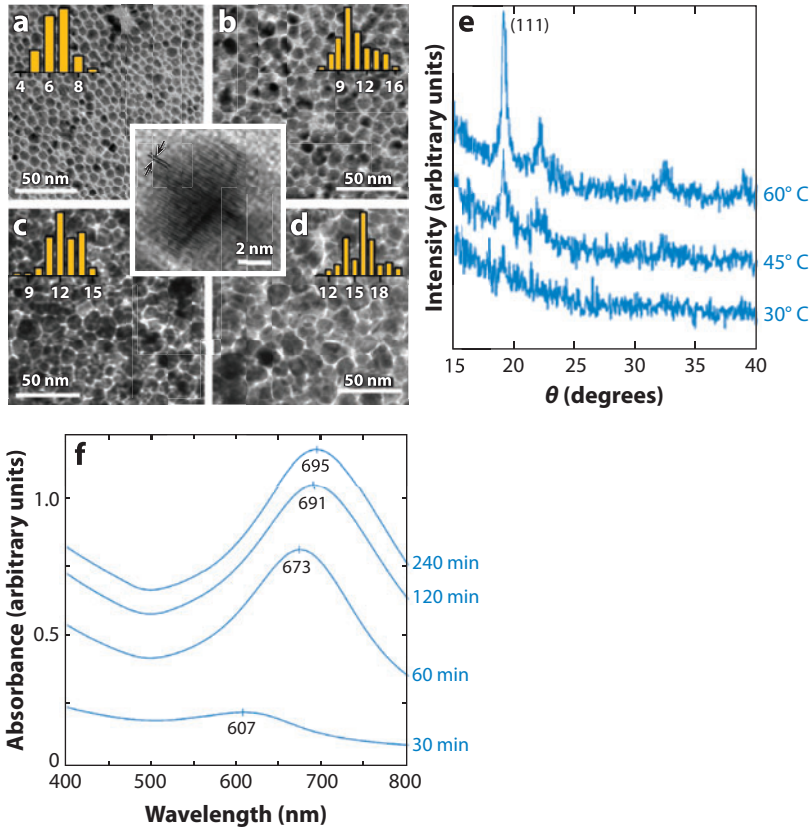

Figure 10

Transmission electron microscopy (TEM) images of ultrathin nanocrystalline Au films comprise close-packed arrays of nanocrystals prepared at the liquid-liquid interface at (*a*) 30° C, (*b*) 45° C, (*c*) 60° C, and (*d*) 75° C. With an increase in temperature, particles of uneven shapes and sizes tend to form, some of them exhibiting multiply twinned structures. The histograms shown alongside the TEM images reveal that the size range of the nanocrystals increases progressively with the increase in temperature. (*Inset*) A high-resolution TEM (HREM) image of an individual particle shows distinct (111) planes with a separation of ~2.3 Å. (*e*) X-ray diffraction (XRD) patterns of nanocrystalline Au films obtained at different temperatures. Although the films obtained at 45° C and 60° C exhibit prominent (111) peaks ($d = 2.33$ Å), the film obtained at 30° C shows weak and broad reflections due to the small particle size. (*f*) Evolution of electronic absorption spectra with growth of nanocrystalline Au films at the interface. The Au films exhibit a strong plasmon absorption band around 700 nm. Note that the plasmon absorption band is observed at ~530 nm in colloidal Au nanocrystals in solution. The position and the intensity of the plasmon band in nanocrystal assemblies are indicative of the nanocrystals' state of aggregation. Reprinted from Reference 19 with permission. Copyright 2005, American Chemical Society.

nanohelics has been carried out by Wang and coworkers (56). **Figure 13** shows Wang et al.'s TEM images of distinctive helical structures of ZnO made of a superlattice-structured nanobelt formed spontaneously in a solid-vapor growth process. The superlattice nanobelt is a periodic, coherent, epitaxial, and parallel growth of two alternating nanostripes of ZnO crystals oriented with their *c* axes perpendicular to each other. The ED pattern from a single period of a nanohelix shows

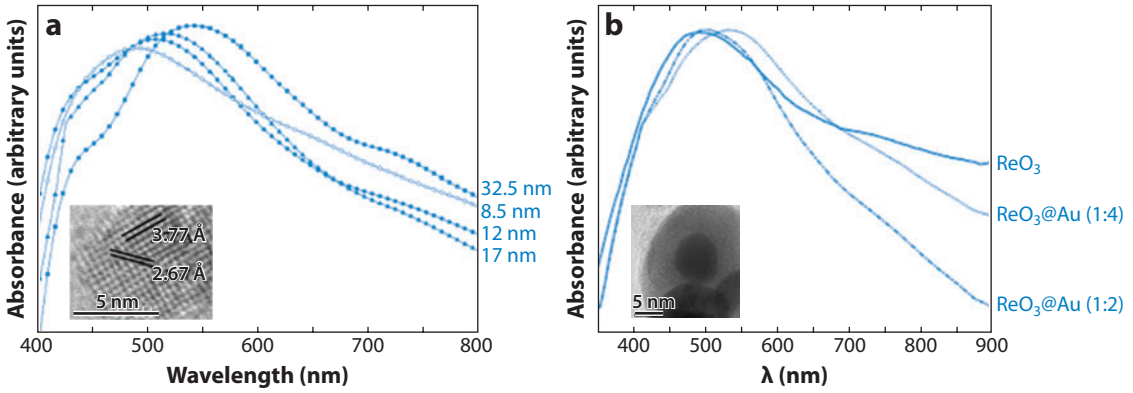

Figure 11

(*a*) Ultraviolet (UV)-visible absorption spectra of ReO_3 nanocrystals with average diameters of 8.5, 12, 17, and 32.5 nm. (*Inset*) A high-resolution transmission electron microscopy (HREM) image of single 8.5-nm ReO_3 nanocrystals. The lattice spacings of 3.77 Å and 2.67 Å correspond to the (100) and (110) interplanar distances, respectively. (*b*) UV-visible absorption spectra of ReO_3@Au core-shell nanocrystals (1:2 and 1:4). (*Inset*) HREM image of ReO_3@Au formed over an 8.5-nm ReO_3 particle. Reprinted from References 7 and 51 with permission. Copyright 2006, American Chemical Society; copyright 2007, Royal Society of Chemistry.

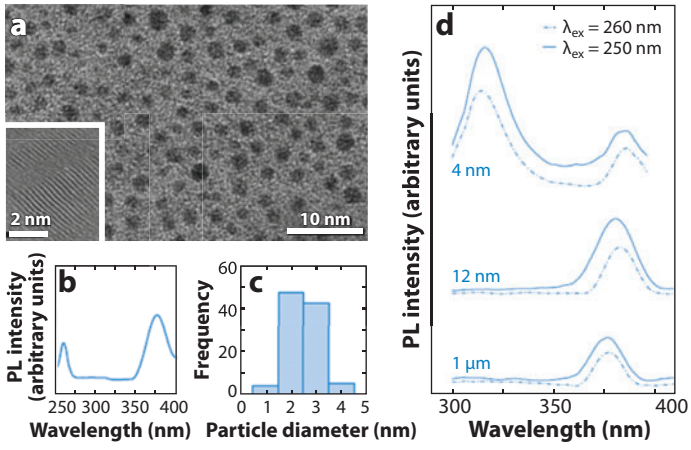

Figure 12

(*a*) Transmission electron microscopy (TEM) image of *N*-cetyl-*N*,*N*,*N*-trimethylammonium bromide (CTAB)-capped 2.5-nm GaN nanocrystals prepared with Ga cupferron. (*Inset*) High-resolution TEM (HTEM) image. (*b*) Photoluminescence (PL) spectrum of CTAB-capped 2.5-nm GaN nanocrystals. The spectrum shows bands centered at 375 nm and 265 nm under an excitation wavelength of 235 nm. The 265-nm blueshifted band corresponds to the 315-nm band exhibited by the ~4-nm particles in panel *d*. (*c*) The particles' size distribution. (*d*) PL spectra of 4-nm, 12-nm, and 1-μm GaN nanocrystals. Although the 12-nm and 1-μm crystals' spectra show a broad band around 375 nm at excitation wavelengths of 250 and 260 nm, the 4-nm nanocrystals show an additional band around 315 nm, which is believed to be a signature of quantum confinement. The 375-nm band is insensitive to particle size. Reprinted from Reference 53 with permission. Copyright 2004, Wiley-VCH Verlag.

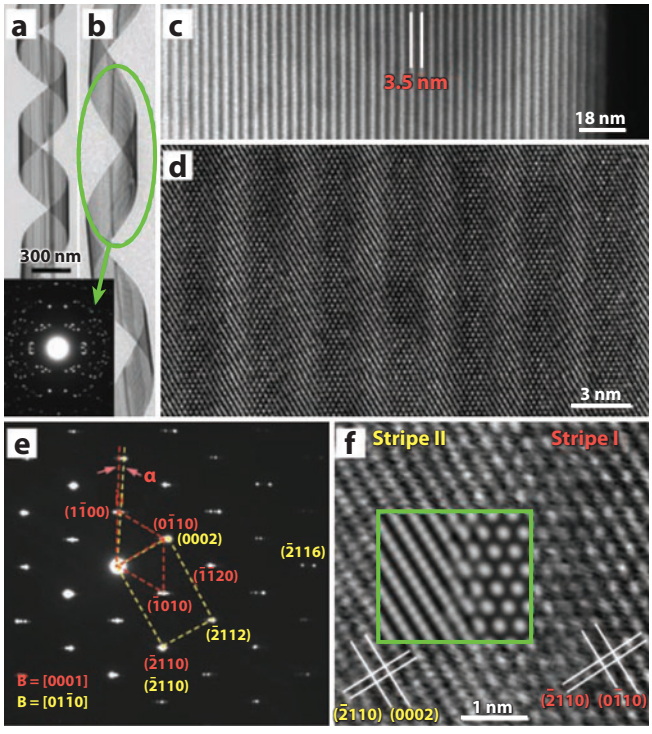

Figure 13

(*a*) Typical low-magnification transmission electron microscopy (TEM) image of a ZnO nanohelix, showing its structural uniformity. (*b*) Low-magnification TEM image of a ZnO nanohelix with a larger pitch-to-diameter ratio. The selected area electron diffraction (SAED) pattern (*inset*) is from a full turn of the helix. (*c*) Dark-field TEM image from a segment of a nanohelix. The edge at the right and side is the edge of the nanobelt, which has a periodic superlattice structure across its entire width with a periodicity of ~3.5 nm. With a 5° offset, the stripes are parallel to the growth direction and run along the length of the nanohelix. (*d*) High-resolution TEM (HREM) image of a ZnO nanohelix with the incident beam perpendicular to the surface of the nanobelt. The lattice structure of the two alternating stripes is visible. (*e*) SAED pattern corresponding to the image in panel *d*. The ED pattern of the nanobelt shows that the growth directions of the two types of stripes have a rotation of $\alpha \sim 4°$, indicating that the adjacent stripes rotate in the plane of the nanobelt for the same magnitude of the angle when forming the superlattice. (*f*) Enlarged HREM image showing the interface between the two adjacent stripes. Reprinted from Reference 56 with permission. Copyright 2005, AAAS.

mirror symmetry. The mirror symmetry is caused by superposition of several ZnO diffraction patterns rotated around the axial direction of the nanohelix.

Aligned ZnO nanowires have been explored for stimulated emission by measuring the excitation density-dependent emission (57). Light emission collected in the direction normal to the end surface plane (along the *c* axis) of the nanowires reveals lasing in the absence of any mirrors with increasing pump power (**Figure 14**).

An AFM-based technique has been utilized for measuring the elastic modulus of individual ZnO nanowires aligned on a solid substrate without destroying or manipulating the sample (58). By simultaneously acquiring the topography and lateral force image of the aligned nanowire, the elastic modulus of individual nanowires can be derived (**Figure 15**). The measurement is based

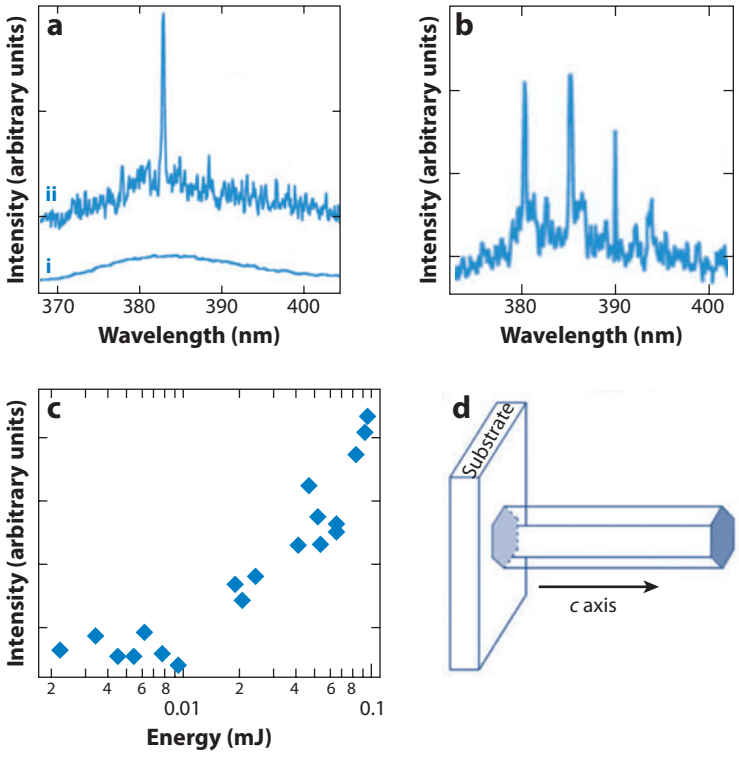

Figure 14

(*a*) Emission spectra from ZnO nanowire arrays below (*i*) and above (*ii* and *b*) the lasing threshold. The pump powers for these spectra are 20, 100, and 150 kW cm^{-2}, respectively. (*c*) Integrated emission intensity from nanowires as a function of optical pumping energy intensity. (*d*) Schematic illustration of a nanowire as a resonance cavity. Reprinted from Reference 57 with permission. Copyright 2001, AAAS.

on quantifying the lateral force required to induce the maximal deflection of the nanowire, where the AFM tip scans over the surface in contact mode.

A strain-induced conductance transition in ZnO nanowire has been studied by a four-tip STM (59). **Figure 16** shows the procedure for the *I–V* measurements. Researchers have found that after bending the nanowire with the STM, the conductance is reduced by five orders of magnitude. These studies demonstrate that strain has a strong effect on the alignment of the Fermi level and the electron states of defects in ZnO nanowires, whose surfaces contain a large number of defects.

Omega-shaped-gate nanowire-based field effect transistors with channels composed of ZnO nanowires have been fabricated by photolithography (60). The hydrogen- and ethanol-sensing characteristics of thick films of ZnO nanocrystals, nanorods, nanowires, and nanotubes impregnated with Pt have also been studied (61, 62). Growth kinetics of both uncapped and PVP-capped ZnO nanorods have been investigated with a combination of TEM and SAXS to obtain direct information on time-dependent changes in size and shape (63).

3.2.2. Ni and Co. Single-crystalline Ni and Co nanowires fabricated by electrodeposition using anodic aluminum oxide as the template exhibit excellent magnetic properties such as large

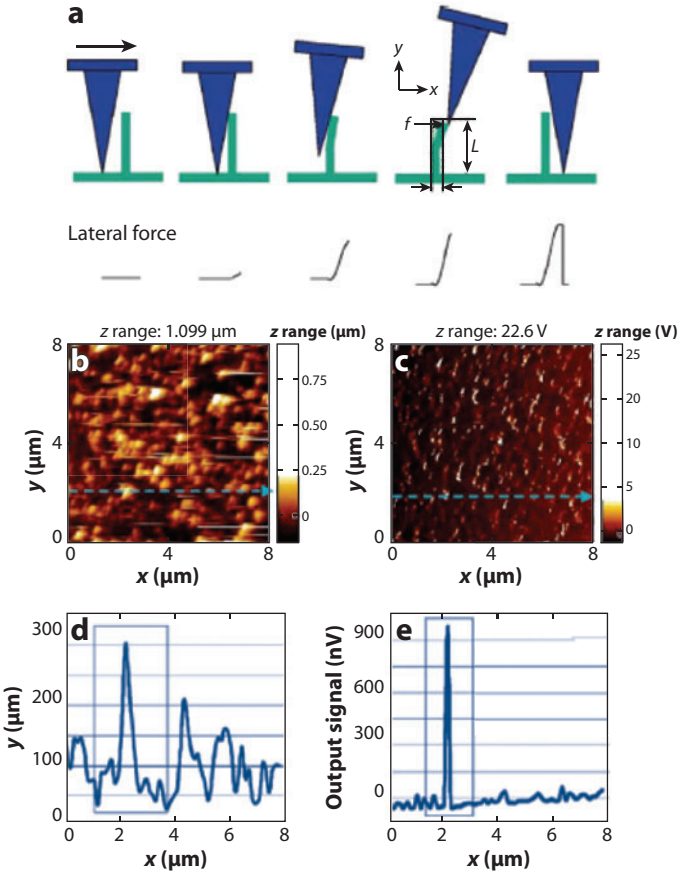

Figure 15

(*a*) Procedures for measuring the elastic modulus of aligned ZnO nanowire arrays in atomic force microscopy (AFM) contact mode. (*b*) Topography image and (*c*) lateral force image of the aligned ZnO nanowires received in AFM contact mode. (*d*, *e*) Line scanning profile along the dashed lines in panels *b* and *c*, respectively. Reprinted from Reference 58 with permission. Copyright 2007, Royal Society of Chemistry.

anisotropy, large coercivity, and high remanence (64). Ni- and Co-homogeneous nanowires show typical anisotropic magnetoresistance of approximately 1.0% (65).

3.2.3. Inorganic nanotubes. Layered inorganic compounds such as boron nitride, metal dichalcogenides, halides, and oxides can form nanotubes (66). Inorganic nanotubes are mainly characterized by TEM (**Figure 17**) (67–70).

3.2.4. Carbon nanotubes. Ever since the discovery of carbon nanotubes, several means of characterizing them have been explored. Raman spectroscopy has provided important insights into the structure of carbon nanotubes. Studies of single-walled carbon nanotubes (SWNTs) by Dresselhaus and coworkers (71) reveal many of the characteristic normal modes of an armchair (*n*, *n*) carbon nanotube and show a diameter-selective resonance behavior (**Figure 18**).

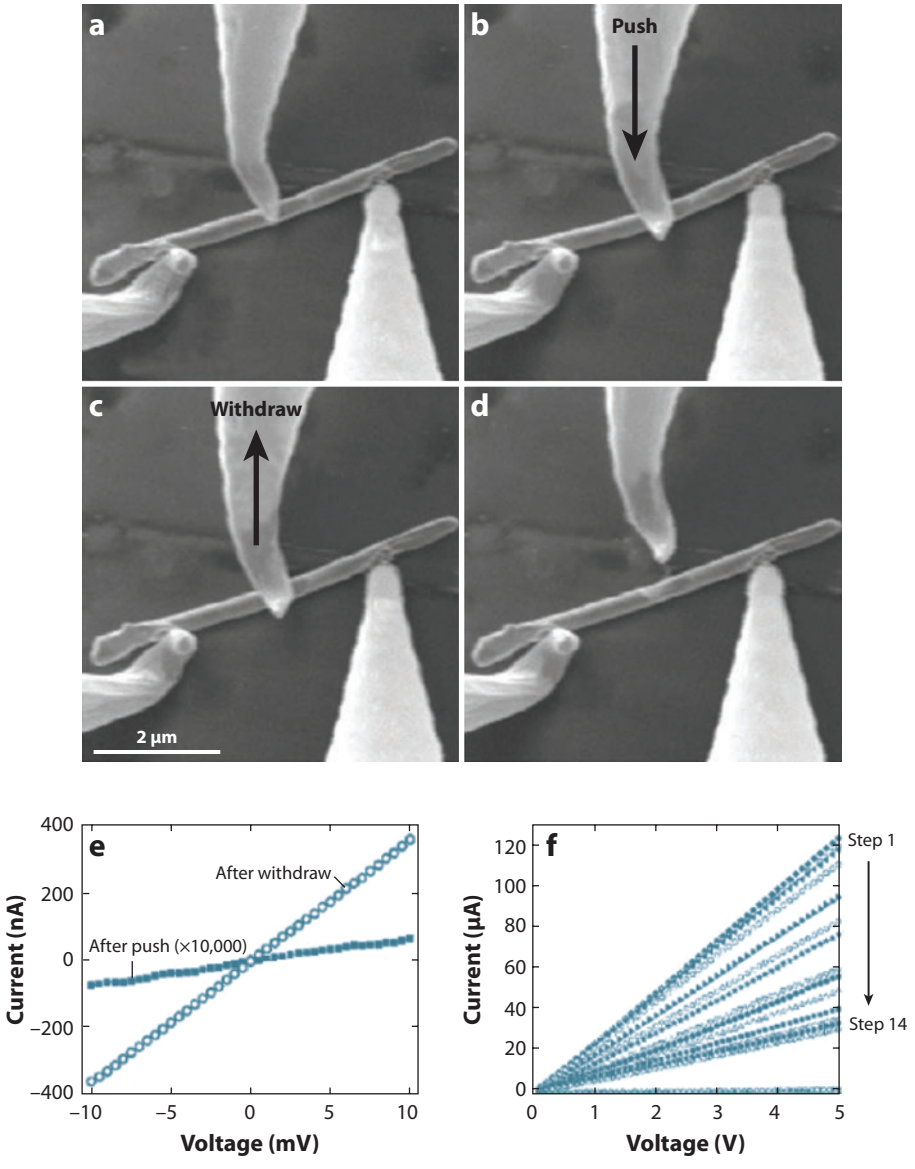

Figure 16

Intrinsic current–voltage (*I–V*) studies of a ZnO nanowire by four-probe scanning tunneling microscopy. (*a*) Two outer tips fix the nanowire and measure the *I–V* curves. (*b*) The middle probe pushes down and bends the nanowire. (*c*) The middle tip retracts and loosens the nanowire. (*d*) The middle tip moves away. (*e*) The curve indicated by filled rectangles corresponds to panel *b*; the curve indicated by empty circles corresponds to panel *c*. (*f*) Results from another experiment that pushed the nanowire with several small steps. Shown are the corresponding *I–V* curves after each step. Reprinted from Reference 59 with permission. Copyright 2006, American Institute of Physics.

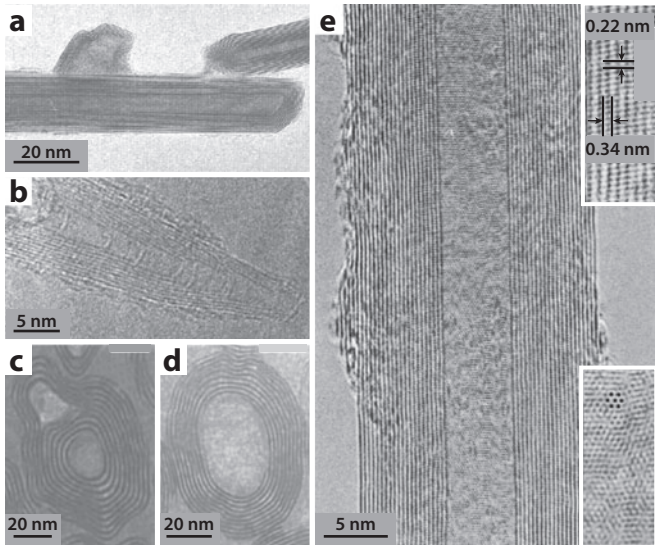

Figure 17

High-resolution transmission electron microscopy (HREM) images of (*a*) WS_2 and (*b*) GaSe nanotubes. Cross-sectional transmission electron microscopy (TEM) images of different types of VO_x nanotube with interacted amines of varying chain lengths: (*c*) C_{16}-VO_x nanotubes show single-layer scrolls with narrow cores and thick walls composed of several vanadium oxide layers. (*d*) Double-layer scroll of C_{20}-DA-VO_x nanotubes obtained from C_{16}-VO_x nanotubes by a template exchange reaction with dodecyldiamine. (*e*) HREM image of a BN multiwalled nanotube with uniform layer separation of 0.34 nm. The layered structures are similar to those in carbon nanotubes. (*Upper right inset*) The atomic columns in the wall fragments show lattice fringes separated by an average of ~0.22 nm and an angle of 12.5° with respect to the tube axis, exhibiting *r*-BN stacking order. (*Lower right inset*) The hexagonal fringes of $10\bar{1}0$ spacing in the core region. Reprinted from References 67–70 with permission. Copyright 2000, 2005, 1999, and 2001, American Chemical Society.

Electronic absorption spectra of SWNTs show transitions in the visible and near-infrared regions (**Figure 19**) (72). Due to their one-dimensional nature, carbon nanotubes exhibit van Hove singularities in the electronic density of states (73); visible–near-infrared spectroscopy provides evidence for supporting their one-dimensional nature. The first and second peaks arise from S_{11} and S_{22} transitions of the semiconducting nanotubes, and the third peak is due to the M_{11} transition of the metallic nanotubes. STM has been used to elucidate the unique structural and electronic properties of SWNTs (74).

3.3. Two-Dimensional Graphene

Graphene refers to a flat monolayer of carbon atoms tightly packed into a two-dimensional honeycomb lattice; it is a basic building block of graphitic materials of all other dimensionalities. Graphene has been characterized with various microscopic and spectroscopic techniques (75). AFM is one of the basic characterization tools for graphene and provides information about the numbers of layers present in the sample (**Figure 20*a***) (76). TEM has been proven to determine the number of layers as well as the structure of graphene (**Figure 20*b***) (77), as has STM (**Figure 20*c***) (78), XRD (**Figure 20*d***) (79, 80), and Raman (**Figure 20*e***) (81).

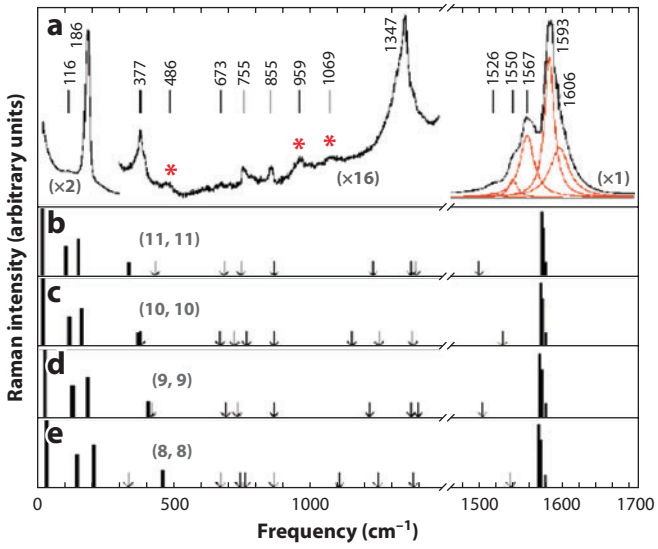

Figure 18

(*a*) Raman spectra showing the diameter-dependent scattering in single-walled nanotubes. An asterisk in the spectrum refers to a feature assigned tentatively to second-order Raman scattering. The five red curves shown in panel *a* are the individual Raman modes that were obtained after deconvolution of the broad experimental peak (*black curve*). (*b–e*) Calculated Raman spectra for armchair (*n*, *n*) nanotubes ($n = 8$–11). The downward-pointing arrows indicate the positions of the remaining weak, Raman-active modes. The strongest experimentally observed band is a graphite band that splits into bands at 1567 and 1592 cm^{-1}. The 1347-cm^{-1} band is the diamond band that arises from sp^3 carbon. The band at 186 cm^{-1} arises from the radial breathing mode of SWNT, and it is diameter dependent. Reprinted from Reference 71 with permission. Copyright 1997, AAAS.

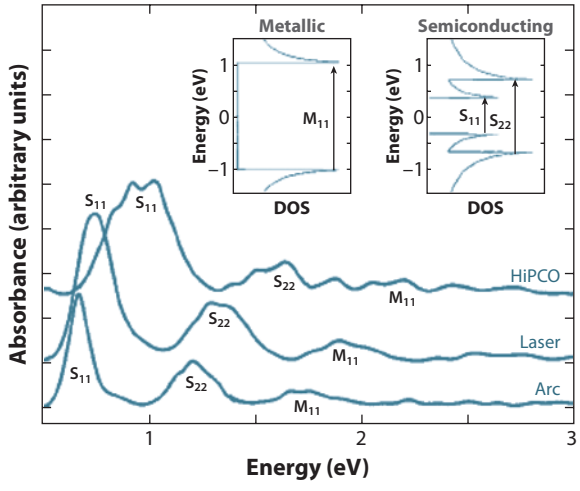

Figure 19

Absorption spectra of purified HiPCO–, purified Laser–, and soluble Arc–produced single-walled nanotubes after baseline correction. Abbreviation: DOS, density of states. Reprinted from Reference 72 with permission. Copyright 2001, American Chemical Society.

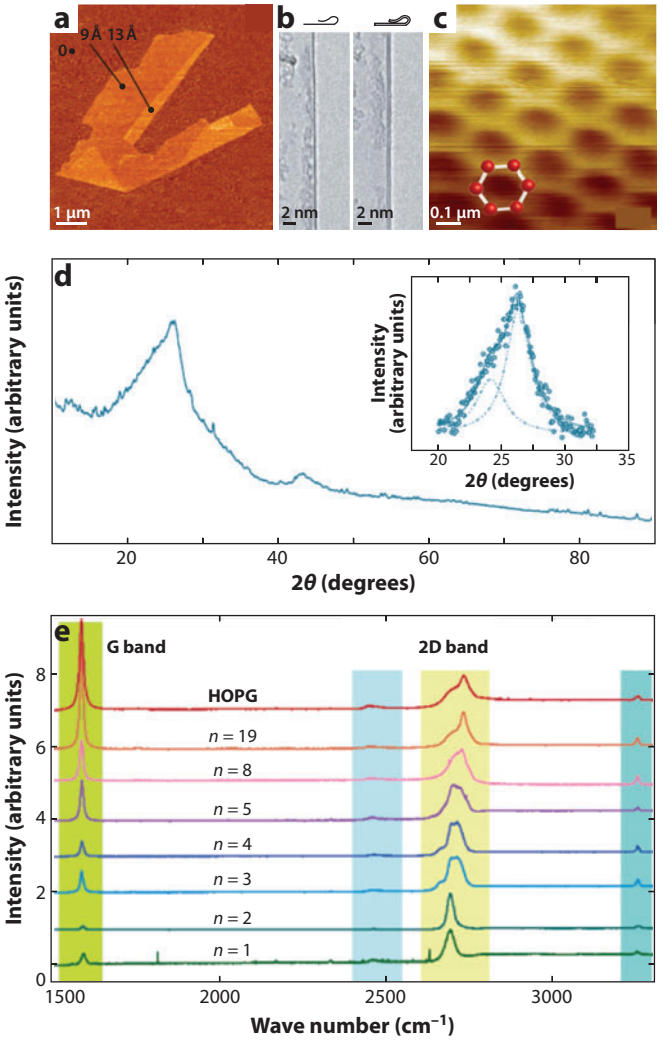

Figure 20

(*a*) Atomic force microscopy (AFM) image of single-layer graphene. The folded edge exhibiting a relative height of ~4 Å clearly indicates that the graphene comprises a single layer. (*b*) Transmission electron microscopy (TEM) images of folded edges of monolayer and bilayer graphene. A folded graphene sheet is locally parallel to the electron beam and, for monolayer graphene, a fold exhibits only one dark line (*left panel*), similar to TEM images from one half of a single-walled carbon nanotube. For comparison, the right panel shows a folded edge of bilayer graphene that exhibits two dark lines, as in the case of double-walled nanotubes. (*c*) High-resolution scanning tunneling microscopy (STM) images of single-layer graphene over a 1-nm^2 area. In the regions that were identified as consisting of single-layer graphene, a honeycomb structure can be observed. (*d*) X-ray diffraction (XRD) pattern of few-layer graphene. The broad peak around 25° is due to the (002) reflection of graphene. (*Inset*) Double Lorenzian fit for (002) reflection. The average number of layers is found to be four. (*e*) Raman spectrum of graphene with an increasing number of layers (n = 1–19) supported on a SiO_2:Si substrate along with highly oriented pyrolitic graphite (HOPG) (n = infinity). Reprinted from References 76, 77, 78, and 81 with permission. Copyright 2005, National Academy of Science USA; copyright 2007, Nature Publishing Group; copyright 2007, National Academy of Science USA; and copyright 2006, American Chemical Society.

SUMMARY POINTS

1. Although XRD can provide information about the gross crystal structure of nanomaterials, TEM provides not only direct information about size and shape but also structural information. The resolution of the SEM is not high compared to that of TEM, but SEM can image larger areas.
2. Scanning probe microscopies provide information about the morphology as well as the electronic states of nanomaterials of different dimensionalities.
3. SAXS is a useful technique for determining the sizes and shapes of nanocrystals in dilute dispersions. SAXS is most effective for in situ study of the growth of nanocrystals.
4. EDAX and EELS are both useful for the elemental analysis of nanomaterials. EELS has certain advantages over the EDAX and can differentiate different allotropes of carbon. EELS can also provide information about the electronic structure of nanomaterials.
5. Raman spectroscopy is an important tool for the characterization of nanomaterials, especially carbon nanotubes and graphene.
6. Electronic absorption spectra and PL spectra are essential for obtaining information about the electronic structure of nanomaterials and the size dependence of the electronic structure.
7. We have illustrated the use of a combination of techniques in the cases of Au, ReO_3, and GaN nanocrystals; ZnO nanowires and nanorods; carbon nanotubes; and graphene.

FUTURE ISSUES

1. There are several challenges to developing better techniques for the characterization of nanomaterials. Improved resolution of microscopic and spectroscopic techniques will provide valuable insights into the properties of nanomaterials.
2. There are certain materials for which characterization is not straightforward. For example, exact methods of characterization of graphene with more than one layer need to be explored.
3. Aspects of nanomaterials such as self-assembly and reactions at the nanoscale can be studied with improved physical techniques.

DISCLOSURE STATEMENT

The authors are not aware of any affiliations, memberships, funding, or financial holdings that might be perceived as affecting the objectivity of this review.

ACKNOWLEDGMENTS

We apologize in advance to all the investigators whose research could not be cited owing to the requirement of brevity.

LITERATURE CITED

1. Kaufmann EN, ed. 2003. *Characterization of Materials*, 2 vol. Hoboken, NJ: Wiley
2. Nanostructure and function (characterization of local nanostructure). 2007. In *Nanoparticle Technology Handbook*, ed. M Hosokawa, K Nogi, N Naito, T Yokoyama, pp. 269–312. Amsterdam: Elsevier. 1st ed.
3. Rietveld HM. 1969. A profile refinement method for nuclear and magnetic structures. *J. Appl. Crystallogr.* 2:65–71
4. Tolbert SH, Alivisatos AP. 1994. Size dependence of a first order solid-solid phase transition: the wurtzite to rock salt phase transformation in CdSe nanocrystals. *Science* 265:373–76
5. Ghosh M, Biswas K, Sundaresan, Rao CNR. 2006. MnO and NiO nanocrystals: synthesis and magnetic properties. *J. Mater. Chem.* 16:106–11
6. Ghosh M, Sampathkumaran EV, Rao CNR. 2005. Synthesis and magnetic property of CoO nanocrystals. *Chem. Mater.* 16:2348–52
7. Biswas K, Rao CNR. 2006. Metallic ReO_3 nanocrystals. *J. Phys. Chem. B* 110:842–45
8. Williams B, Carter CB. 1997. *Transmission Electron Microscopy*. New York: Plenum
9. Park J, An K, Hwang Y, Park JG, Noh HJ, et al. 2004. Ultra-large-scale syntheses of monodisperse nanocrystal. *Nat. Mater.* 3:891–95
10. Manna L, Scher EC, Alivisatos AP. 2000. Synthesis of soluble and processable rod-, arrow-, teardrop-, and tetrapod-shaped CdSe nanocrystals. *J. Am. Chem. Soc.* 122:12700–6
11. Iijima S, Ichihashi T. 1993. Single-shell carbon nanotubes of 1-nm diameter. *Nature* 363:603–5
12. Iijima S. 1991. Helical microtubules of graphitic carbon. *Nature* 354:56–58
13. Hirahara K, Suenaga K, Bandow S, Kato H, Okazaki T, et al. 2000. One-dimensional metallofullerene crystal generated inside single-walled carbon nanotubes. *Phys. Rev. Lett.* 85:5384–87
14. Egerton RF. 1996. *Electron Energy-Loss Spectroscopy in the Electron Microscope*. New York: Plenum
15. Sen R, Satishkumar BC, Govindaraj A, Harikumar KR, Raina G, et al. 1998. B–C–N, C–N and B–N nanotubes produced by the pyrolysis of precursor molecules over Co catalysts. *Chem. Phys. Lett.* 287:671–76
16. Satishkumar BC, Govindaraj A, Harikumar KR, Zhang JP, Cheetham AK, Rao CNR. 1999. Boron-carbon nanotubes from the pyrolysis of C_2H_2-B_2H_6 mixtures. *Chem. Phys. Lett.* 300:473–77
17. Goldstein J, Newbury D, Joy D, Lyman C, Echlin P, et al. 2003. *Scanning Electron Microscopy and X-Ray Microanalysis*. New York: Springer. 3rd ed.
18. Samori P, ed. 2006. *Scanning Probe Microscopies Beyond Imagining: Manipulation of Molecules and Nanostructures*. Weinheim, Ger.: Wiley-VCH Verlag
19. Agrawal VV, Kulkarni GU, Rao CNR. 2005. Nature and properties of ultrathin nanocrystalline gold films formed at the organic-aqueous interface. *J. Phys. Chem. B* 109:7300–5
20. Thomas PJ, Kulkarni GU, Rao CNR. 2004. Dip-pen lithography using aqueous metal nanocrystal dispersions. *J. Mater. Chem.* 14:625–28
21. Rout CS, Kulkarni GU, Rao CNR. 2007. Room temperature hydrogen and hydrocarbon sensors based on single nanowires of metal oxides. *J. Phys. D: Appl. Phys.* 40:2777–82
22. Thomas PJ, Kulkarni GU, Rao CNR. 2000. Effect of size on the Coulomb staircase phenomenon in metal nanocrystals. *Chem. Phys. Lett.* 321:163–68
23. Deepak FL, John NS, Govindaraj A, Kulkarni GU, Rao CNR. 2005. Nature and electronic properties of Y-junctions in CNTs and N-doped CNTs obtained by the pyrolysis of organometallic precursors. *Chem. Phys. Lett.* 411:468–73
24. Pedersen JS. 1997. Analysis of small-angle scattering data from colloids and polymer solutions: modeling and least-squares fitting. *Adv. Colloid Interface Sci.* 70:171–210
25. Pedersen JS. 2002. Modelling of small-angle scattering data from colloids and polymer systems. In *Neutrons, X-Rays and Light: Scattering Methods Applied to Soft Condensed Matter*, ed. P Lindner, Th Zemb, pp. 391–420. Amsterdam: Elsevier
26. Murray CB, Kagan CR, Bawendi MG. 2000. Synthesis and characterization of monodisperse nanocrystals and close-packed nanocrystal assembly. *Annu. Rev. Mater. Sci.* 30:545–610

27. Billinge SJL, Kanatzidis. 2004. Beyond crystallography: the study of disorder, nanocrystallinity and crystallographically challenged materials with pair distribution functions. *Chem. Commun.* 749–60
28. Page K, Proffen TH, Humberto T, Terrones M, Lee L, et al. 2004. Direct observation of the structure of gold nanocrystals by total scattering powder neutron diffraction. *Chem. Phys. Lett.* 393:385–88
29. Agrawal VV, Mahalakshmi P, Kulkarni GU, Rao CNR. 2006. Nanocrystalline films of Au-Ag, Au-Cu, and Au-Ag-Cu alloys formed at the organic-aqueous interface. *Langmuir* 22:1846–51
30. Yu WW, Qu L, Guo W, Peng X. 2003. Experimental determination of the extinction coefficient of CdTe, CdSe, and CdS nanocrystals. *Chem. Mater.* 15:2854–60
31. Varghese N, Biswas K, Rao CNR. 2008. Investigations of the growth kinetics of capped CdSe and CdS nanocrystals by a combined use of small-angle X-ray scattering and other techniques. *Chem. Asian J.* 3:1435–42
32. Peng X, Wickham J, Alivisatos AP. 1998. Kinetics of II-VI and III-V colloidal semiconductor nanocrystal growth: "focusing" of size distributions. *J. Am. Chem. Soc.* 120:5343–44
33. Ferraro JR, Nakamoto K. 1994. *Introductory Raman Spectroscopy*. San Diego: Academic
34. Dresselhaus MS, Eklund PC. 2000. Phonons in carbon nanotubes. *Adv. Phys.* 49:705–814
35. Tian Z-Q, Ren B, Wu D-Y. 2002. Surface-enhanced Raman scattering: from noble to transition metals and from rough surfaces to ordered nanostructures. *J. Phys. Chem. B* 106:9463–83
36. Sundaresan A, Bhargavi R, Rangarajan N, Siddesh U, Rao CNR. 2006. Ferromagnetism as a universal feature of nanocrystals of the otherwise nonmagnetic oxides. *Phys. Rev. B* 74:161306
37. Madhu C, Sundaresan A, Rao CNR. 2008. Room-temperature ferromagnetism in undoped GaN and CdS semiconductor nanocrystals. *Phys. Rev. B* 77:201306
38. Ghosh S, Ramanathan KV, Sood AK. 2004. Water at nanoscale confined in single-walled carbon nanotubes studied by NMR. *Europhys. Lett.* 65:678–84
39. Varghese N, Vivekchand SRC, Govindaraj A, Rao CNR. 2008. A calorimetric investigation of the assembly of gold nanorods to form necklaces. *Chem. Phys. Lett.* 450:340–44
40. Das A, Sood AK, Maiti PK, Das M, Varadarajan R, Rao CNR. 2008. Binding of nucleobases with single-walled carbon nanotubes: theory and experiment. *Chem. Phys. Lett.* 453:266–73
41. Jana NR, Peng X. 2003. Single-phase and gram-scale routes toward nearly monodisperse Au and other noble metal nanocrystals. *J. Am. Chem. Soc.* 125:14280–81
42. Kim F, Song JH, Yang P. 2002. Photochemical synthesis of gold nanorods. *J. Am. Chem. Soc.* 124:14316–17
43. Xiao Y, Shlyahovsky B, Popov I, Pavlov V, Willner I. 2005. Shape and color of Au nanocrystals follow biocatalytic processes. *Langmuir* 21:5659–62
44. Link S, El-Sayed MA. 2000. Shape and size dependence of radiative, nonradiative and photothermal properties of gold nanocrystals. *Int. Rev. Phys. Chem.* 19:409–53
45. Link S, El-Sayed MA. 2003. Optical properties and ultrafast dynamics of metallic nanocrystals. *Annu. Rev. Phys. Chem.* 54:331–66
46. Burda C, Chen X, Narayanan R, El-Sayed MA. 2005. Chemistry and properties of nanocrystals of different shapes. *Chem. Rev.* 105:1025–102
47. Biswas K, Varghese N, Rao CNR. 2008. Growth kinetics of gold nanocrystals: a combined small angle X-ray scattering and calorimetric study. *Small* 4:649–55
48. Viswanatha R, Sarma DD. 2007. Growth of nanocrystals in solution. In *Nanomaterials Chemistry: Recent Developments and New Directions*, ed. CNR Rao, A Muller, AK Cheetham, 4:169–70. Weinheim, Ger.: Wiley-VCH
49. Rao CNR, Raveau B. 1995. *Transition Metal Oxides*. Weinheim, Ger.: Wiley-VCH. 2nd ed.
50. Biswas K, Muthu DVS, Sood AK, Kruger MB, Chen B, Rao CNR. 2007. Pressure-induced phase transitions in nanocrystalline ReO_3. *J. Phys. Condens. Matter* 19:436214
51. Ghosh S, Biswas K, Rao CNR. 2007. Core-shell nanocrystals based on an oxide metal: ReO_3@Au (Ag) and ReO_3@SiO_2 (TiO_2). *J. Mater. Chem.* 17:2412–17
52. Biswas K, Bhat SV, Rao CNR. 2007. Surface-enhanced Raman spectra of aza-aromatics on nanocrystals of metallic ReO_3. *J. Phys. Chem. C* 111:5689–93

53. Sardar K, Rao CNR. 2004. New solvothermal routes for GaN nanocrystals. *Adv. Mater.* 16:425–29
54. Biswas K, Sardar K, Rao CNR. 2006. Ferromagnetism in Mn-dopped GaN nanocrystals prepared solvothermally at low temperatures. *App. Phys. Lett.* 89:132503
55. Klingshirn C. 2007. ZnO: material, physics and applications. *Chem. Phys. Chem.* 8:782–803
56. Gao PX, Ding Y, Mai W, Hughes WL, Lao C, Wang ZL. 2005. Conversion of zinc oxide nanobelts into superlattice-structured nanohelices. *Science* 309:1700–4
57. Huang MH, Mao S, Feick H, Yan H, Wu Y, et al. 2001. Room-temperature UV nanowire nanolasers. *Science* 292:1897–99
58. Wang X, Song J, Wang ZL. 2007. Nanowire and nanobelt arrays of zinc oxide from synthesis to properties and to novel devices. *J. Mater. Chem.* 17:711–20
59. Lin X, He XB, Yang TZ, Guo W, Shi DX, et al. 2006. Intrinsic current-voltage properties of nanowires with four-probe scanning tunneling microscopy: a conductance transition of ZnO nanowire. *Appl. Phys. Lett.* 89:043103
60. Keem K, Jeong D-Y, Kim S, Lee M-S, Yeo I-S, et al. 2006. Fabrication and device characterization of omega-shaped-gate ZnO nanowire field-effect transistors. *Nano Lett.* 6:1454–58
61. Rout CS, Krishna SH, Vivekchand SRC, Govindaraj A, Rao CNR. 2006. Hydrogen and ethanol sensors based on ZnO nanorods, nanowires and nanotubes. *Chem. Phys. Lett.* 418:586–90
62. Rout CS, Raju AR, Govindaraj A, Rao CNR. 2007. Ethanol and hydrogen sensors based on ZnO nanocrystals and nanowires. *J. Nanosci. Nanotech.* 7:1923–29
63. Biswas K, Das B, Rao CNR. 2008. Growth kinetics of ZnO nanorods: capping-dependent mechanism and other interesting features. *J. Phys. Chem. C* 112:2404–11
64. Pan H, Liu B, Yi J, Poh C, Lim S, et al. 2005. Growth of single-crystalline Ni and Co nanowires via electrochemical deposition and their magnetic properties. *J. Phys. Chem. B* 109:3096–98
65. Ohgai T, Hoffer X, Fabian A, Gravier L, Ansermet J-P. 2003. Electrochemical synthesis and magnetoresistance properties of Ni, Co and Co/Cu nanowires in a nanoporous anodic oxide layer on metallic aluminium. *J. Mater. Chem.* 13:2530–34
66. Rao CNR, Nath M. 2003. Inorganic nanotubes. *Dalton Trans.* 1–24
67. Rothschild A, Popovitz-Biro R, Lourie O, Tenne R. 2000. Morphology of multiwall WS_2 nanotubes. *J. Phys. Chem. B* 104:8976–81
68. Gautam UK, Vivekchand SRC, Govindaraj A, Kulkarni GU, Selvi NR, Rao CNR. 2005. Generation of onions and nanotubes of GaS and GaSe through laser and thermally induced exfoliation. *J. Am. Chem. Soc.* 127:3658–59
69. Krumeich F, Muhr H-J, Niederberger M, Bieri F, Schnyder B, Nesper R. 1999. Morphology and topochemical reactions of novel vanadium oxide nanotubes. *J. Am. Chem. Soc.* 121:8324–31
70. Ma R, Bando Y, Sato T, Kurashima K. 2001. Growth, morphology, and structure of boron nitride nanotubes. *Chem. Mater.* 13:2965–71
71. Rao AM, Richter E, Bandow S, Chase B, Eklund PC, et al. 1997. Diameter-selective Raman scattering from vibrational modes in carbon nanotubes. *Science* 275:187–91
72. Hamon MA, Itkis ME, Niyogi S, Alvaraez T, Kuper C, et al. 2001. Effect of rehybridization on the electronic structure of single-walled carbon nanotubes. *J. Am. Chem. Soc.* 123:11292–93
73. Ouyang M, Huang J-L, Lieber CM. 2002. Fundamental electronic properties and applications of single-walled carbon nanotubes. *Acc. Chem. Res.* 35:1018–25
74. Odom TW, Huang J-L, Kim P, Lieber CM. 2000. Structure and electronic properties of carbon nanotubes. *J. Phys. Chem. B* 104:2794–809
75. Geim AK, Novoselov KS. 2007. The rise of graphene. *Nat. Mater.* 6:183–91
76. Novoselov KS, Jiang D, Schedin F, Booth TJ, Khotkevich VV, et al. 2005. Two-dimensional atomic crystals. *Proc. Natl. Acad. Sci. USA* 102:10451–53
77. Meyer JC, Geim AK, Katsnelson MI, Novoselov KS, Booth TJ, Roth S. 2007. The structure of suspended graphene sheets. *Nature* 446:60–63
78. Stolyarova E, Taeg RK, Ryu S, Maultzsch J, Kim P, et al. 2007. High-resolution scanning tunneling microscopy imaging of mesoscopic graphene sheets on an insulating surface. *Proc. Natl. Acad. Sci. USA* 104:9209–12

79. Rao CNR, Biswas K, Subramanyam KS, Govindaraj A. 2008. Graphene, the new nanocarbon. *J. Mater. Chem.* 19:2457–69
80. Subrahmanyam KS, Vivekchand SRC, Govindaraj A, Rao CNR. 2008. A study of graphenes prepared by different methods: characterization, properties and solubilisation. *J. Mater. Chem.* 18:1517–23
81. Gupta A, Chen G, Joshi P, Tadigadapa S, Eklund PC. 2006. Raman scattering from high-frequency phonons in supported n-graphene layer films. *Nano Lett.* 6:2667–73

Annual Review of
Analytical Chemistry

Volume 2, 2009

Contents

A Conversation with John B. Fenn
John B. Fenn and M. Samy El-Shall 1

Liquid-Phase and Evanescent-Wave Cavity Ring-Down Spectroscopy in Analytical Chemistry
L. van der Sneppen, F. Ariese, C. Gooijer, and W. Ubachs 13

Scanning Tunneling Spectroscopy
Harold J. W. Zandvliet and Arie van Houselt 37

Nanoparticle PEBBLE Sensors in Live Cells and In Vivo
Yong-Eun Koo Lee, Ron Smith, and Raoul Kopelman 57

Micro- and Nanocantilever Devices and Systems for Biomolecule Detection
Kyo Seon Hwang, Sang-Myung Lee, Sang Kyung Kim, Jeong Hoon Lee, and Tae Song Kim 77

Capillary Separation: Micellar Electrokinetic Chromatography
Shigeru Terabe 99

Analytical Chemistry with Silica Sol-Gels: Traditional Routes to New Materials for Chemical Analysis
Alain Walcarius and Maryanne M. Collinson 121

Ionic Liquids in Analytical Chemistry
Renee J. Soukup-Hein, Molly M. Warnke, and Daniel W. Armstrong 145

Ultrahigh-Mass Mass Spectrometry of Single Biomolecules and Bioparticles
Huan-Cheng Chang 169

Miniature Mass Spectrometers
Zheng Ouyang and R. Graham Cooks 187

Analysis of Genes, Transcripts, and Proteins via DNA Ligation
Tim Conze, Alysha Shetye, Yuki Tanaka, Jijuan Gu, Chatarina Larsson, Jenny Göransson, Gholamreza Tavoosidana, Ola Söderberg, Mats Nilsson, and Ulf Landegren 215

Applications of Aptamers as Sensors
Eun Jeong Cho, Joo-Woon Lee, and Andrew D. Ellington 241

Mass Spectrometry–Based Biomarker Discovery: Toward a Global Proteome Index of Individuality
Adam M. Hawkridge and David C. Muddiman 265

Nanoscale Control and Manipulation of Molecular Transport in Chemical Analysis
Paul W. Bohn 279

Forensic Chemistry
Suzanne Bell 297

Role of Analytical Chemistry in Defense Strategies Against Chemical and Biological Attack
Jiri Janata 321

Chromatography in Industry
Peter Schoenmakers 333

Electrogenerated Chemiluminescence
Robert J. Forster, Paolo Bertoncello, and Tia E. Keyes 359

Applications of Polymer Brushes in Protein Analysis and Purification
Parul Jain, Gregory L. Baker, and Merlin L. Bruening 387

Analytical Chemistry of Nitric Oxide
Evan M. Hetrick and Mark H. Schoenfisch 409

Characterization of Nanomaterials by Physical Methods
C.N.R. Rao and Kanishka Biswas 435

Detecting Chemical Hazards with Temperature-Programmed Microsensors: Overcoming Complex Analytical Problems with Multidimensional Databases
Douglas C. Meier, Baranidharan Raman, and Steve Semancik 463

The Analytical Chemistry of Drug Monitoring in Athletes
Larry D. Bowers 485

Errata

An online log of corrections to *Annual Review of Analytical Chemistry* articles may be found at http://anchem.annualreviews.org/errata.shtml